



1 **Relation between the asymmetric ring current effect and the anti-sunward auroral**  
2 **currents, as deduced from CHAMP observations**

3  
4 Hermann Lühr<sup>1)</sup> and Yun-Liang Zhou<sup>2)</sup>

5  
6 1) GFZ, German Research Centre for Geosciences, Section 2.3, Geomagnetism, 14473 Potsdam,  
7 Germany.

8 2) Department of Space Physics, School of Electronic Information, Wuhan University, 430072  
9 Wuhan, China.

10  
11  
12

13 **Abstract.** During magnetically active periods the storm-time disturbance signal on ground  
14 develops commonly an azimuthal asymmetry. Negative deflections of the magnetic horizontal  
15 (H) component are enhanced in the 18:00 local time sector and smallest in the morning sector.  
16 This is commonly attributed to the asymmetric ring current effect. In this study we are  
17 investigating the average characteristics of anti-sunward net currents that are not closing in the  
18 ionosphere. Their intensity is growing proportionally with the amount of solar wind input to the  
19 magnetosphere. There is almost twice as much current flowing in the winter hemisphere as on  
20 the summer side. This seasonal dependence is more pronounced on the dusk than on the dawn  
21 side. Event studies reveal that anti-sunward currents are closely related to the main phase of a  
22 magnetic storm. Since also the asymmetry of storm-time disturbances build up during the main  
23 phase, we suggest a relation between these two phenomena. From a statistical study of ground-  
24 based disturbance levels during magnetically active periods we obtain support for our  
25 suggestion. Observed storm-time disturbance amplitudes are clearly smaller in the summer  
26 hemisphere than in the winter part. This difference increases toward higher latitudes. We propose  
27 a new 3D current system responsible for the zonally asymmetric storm-time disturbance signal  
28 that does not involve the ring current. The high-latitude anti-sunward currents are connected at  
29 their noon and midnight ends to field-aligned currents that lead the currents to the outer  
30 magnetosphere. The net current branch on the morning side is closed along the dawn flank  
31 plasmopause, and the evening side currents along the dusk flank magnetopause. Regardless  
32 through which loop the current is flowing, near-Earth storm-time disturbance level will in both  
33 cases be reduced in the morning sector and enhanced in the evening.

34  
35

36 **1. Introduction**

37 At auroral latitudes intense electric currents are flowing. Due to the anisotropic conductivity  
38 distribution in the ionosphere different current types exist. Quite prominent are the field-aligned



39 currents (FACs), which can transfer energy and momentum over large distances from the  
40 magnetosphere and deposit it in the high-latitude upper atmosphere. Horizontal Pedersen  
41 currents typically closing these FACs in the ionosphere. Furthermore, there are Hall currents,  
42 flowing perpendicular to the electric and magnetic fields. These are generally regarded as source-  
43 free, and they close in the ionosphere.

44 The intensity of currents that close FACs in the ionosphere can be estimated from magnetic field  
45 measurements of low-Earth orbit (LEO) satellites on near-polar orbits. By integrating the along-  
46 track magnetic field component over the full orbit the net current flowing transverse to the  
47 orbital plane can be determined. Corresponding results have been obtained from Magsat (e.g.  
48 Suzuki and Fukushima, 1984), Ørsted (Stauning and Primdahl, 2000) and CHAMP (Zhou and  
49 Lühr, 2017) missions. Net currents up to several Mega Ampère (MA) are observed during  
50 magnetically active periods. In principle there are two types of closure currents. Most prominent  
51 are the cross-polar cap Pedersen currents closing excessive Region 1 (R1) FACs, which are not  
52 balanced by R2 FACs. Somewhat weaker are the anti-sunward net currents connecting excessive  
53 downward FACs on the dayside with upward FACs on the nightside. These anti-sunward  
54 currents, carried predominantly by Hall currents, have first been confirmed observationally from  
55 Magsat data (Suzuki and Fukushima, 1982, 1984). Their intensity is clearly controlled by  
56 magnetic activity. Suzuki and Fukushima (1984) suggested that the anti-sunward current is  
57 closed in the magnetosphere through the partial ring current on the duskside. This may be the  
58 cause for the asymmetric storm-time disturbance signal with clear enhancements in the evening  
59 sector.

60 More recently Zhou and Lühr (2017) provided a detailed study on auroral zone net currents.  
61 Making use of 5 years of high-resolution CHAMP magnetic field data, they could derive the  
62 dependence of these currents on season, solar wind input and solar flux. In particular, by  
63 deriving current estimates separately for the two hemispheres these dependences emerged very  
64 clearly. The cross-polar cap duskward net current peaks at local summer when the ionospheric  
65 conductivity is high. Conversely, the anti-sunward net current attains largest values during local  
66 winter when conductivity gradients between the auroral region and the polar cap maximise, at  
67 which Hall currents can be diverted into FACs. The out-of-phase variation of these two current  
68 types causes quite different responses of net currents in the two hemispheres to magnetic  
69 activity.

70 A still open question is the relationship between auroral zone net currents and the asymmetric  
71 storm-time disturbance during the main phase. Suzuki and Fukushima (1984) proposed a closure



72 of the net anti-sunward current through the duskside partial ring current. It has never been  
73 investigated how the anti-sunward net current flow is split between dawn and dusk side auroral  
74 regions. What is the effect of hemispheric differences in current strength due to seasonal  
75 variation? Can a detailed consideration of all these facts provide hints on the actual 3D geometry  
76 of the net anti-sunward current closure in the magnetosphere?

77 The C/NOFS satellite on its low-inclination orbit can be used to investigate the ring current  
78 asymmetry. On every revolution it samples ring current signals from all local times. Magnetic  
79 field readings of C/NOFS during the years 2008 through 2010 have been considered by Le et al.  
80 (2011) to study the ring current evolution during storms. The authors show that the disturbance  
81 signal is azimuthally symmetric before and after the storm. But during the main phase a clear  
82 asymmetry is building up, with enhanced amplitudes around the 18 LT sector and reduced values  
83 around 06 LT. During the storm recovery phase, the disturbance signal returns to symmetric  
84 distribution. The degree of asymmetry grows as the magnetic activity gets larger, but the local  
85 time sector in which the largest amplitudes are observed stays around 18 LT. Similar results  
86 concerning the asymmetry of the ring current effect have been derived from ground-based  
87 observations (e.g. Love and Gannon, 2009). These authors claim that the dawn-dusk asymmetry  
88 in the disturbance field is on average proportional to  $D_{ST}$ . Newell and Gjerloev (2012) made use  
89 of a large number of magnetometers from the SuperMAG data repository. Their SMR index is  
90 similar to  $D_{ST}$  but provides local time resolution with four sectors (SMR-00, SMR-06, SMR-12,  
91 SMR-18). By means of a superposed epoch analysis Newell and Gjerloev (2012) determined the  
92 response of their index to a magnetic storm. They found a clear dominance of the disturbance  
93 signal at 18 LT and smallest deflections at 06 LT. All this is consistent with the notion of a  
94 partial ring current on the duskside. For checking that inference Lühr et al. (2017) had a look at  
95 *in situ* ring current density measurements by Cluster and other spacecraft. They could not  
96 confirm the enhancement of ring current intensity in the dusk sector. The strongest ring current  
97 parts are rather observed by these missions in the post-midnight sector. The difference in ring  
98 current interpretation from near-Earth observations and *in situ* measurements has been described  
99 in more details by Lühr et al. (2017), but it is still an open issue.

100 A quite different explanation for the asymmetric storm-time disturbance signal during the main  
101 phase was suggested by Crooker and Siscoe (1981). They questioned any connection between  
102 the net current and the ring current. According to their analysis the low-latitude magnetic field  
103 effect of the FACs connecting to the net currents at their noon and midnight ends is sufficient to  
104 generate the observed storm-time asymmetry. Interestingly, they made the statements years



105 before the existence of anti-sunward net currents were observationally confirmed. So far, the  
106 validity of their statements has not been checked in detail.

107 In this study we make use of CHAMP data and follow up on the results presented by Zhou and  
108 Lühr (2017) for addressing the open questions listed above. Of special interest is the relation  
109 between the net anti-sunward current and the asymmetric storm-time effect at low latitudes.  
110 Prime basis for the investigations is the CHAMP magnetic field dataset from the 5 years, 2001-  
111 2005. But also recordings from geomagnetic observatories are taken into account for  
112 characterizing the near-Earth magnetic effects.

113 In the sections to follow we will first shortly introduce the data and basic processing algorithms  
114 for determining net currents. Section 3 presents a statistical survey of net currents at all local  
115 times. The dependence of anti-sunward net currents on solar wind input and season is analysed  
116 in Section 4. Section 5 presents for one magnetic storm a direct comparison between anti-  
117 sunward currents and ground-based disturbance levels. The mean characteristics of the ring  
118 current signal during magnetically active periods ( $K_p > 6$ ), as observed on ground, are outlined  
119 in Section 6. In Section 7 the various observations are discussed, focusing on the comparison  
120 between anti-sunward currents and storm-time disturbance signals. Finally, in Section 8 results  
121 are summarised and a new 3D current system is proposed for closing the anti-sunward net  
122 currents.

123

## 124 **2. Dataset and calculation of net auroral currents**

125 The CHAMP satellite was launched into a near-circular polar orbit (inclination:  $87.3^\circ$ ) with an  
126 initial altitude of 456 km on 15 July 2000 [Reigber et al., 2002]. By the end of the mission, 19  
127 September 2010, the orbit had decayed to 250 km. The orbital plane covers all local times within  
128 130 days when considering upleg and downleg arcs. The Fluxgate Magnetometer (FGM) on  
129 board CHAMP recorded the vector magnetic field every 0.02 s with a resolution of 0.1 nT. The  
130 FGM magnetic field readings are calibrated routinely by using the observations of the onboard  
131 absolute scalar Overhauser Magnetometer. In this study the fully calibrated Level-3 magnetic  
132 field products (product identifier: CH-ME-3-MAG) are used (Rother and Michaelis, 2019),  
133 which are provided in the North-East-Center (NEC) frame with a time resolution of 1 Hz. The  
134 time period used in this study comprises the five years from 2001 to 2005, experiencing solar  
135 and magnetic activities from high to moderate levels. Five years of CHAMP magnetic field  
136 observations are just needed to sample all local times 14 times, evenly distributed over all  
137 seasons.



138 The approach for deriving net currents in the auroral region from CHAMP magnetic field data  
139 has been described in detail by Zhou and Lühr (2017). Here we use the same dataset and adopt  
140 their processing algorithm. Calculations are based on Ampère's law in integral form

$$141 \quad I = \frac{1}{\mu_0} \oint_L B_{AT} dl \quad (1)$$

142 where  $I$  is the net current flowing through the closed integration contour,  $\mu_0$  is the permeability  
143 of the free space,  $B_{AT}$  is the along-track magnetic field component caused by the current  $I$ ,  $dl$  is  
144 a differential path element along the CHAMP orbit. Equation (1) can be written in discrete form  
145 as

$$146 \quad I = \frac{1}{\mu_0} \sum_{m=1}^n B_{ATm} \cdot \Delta l \quad (2)$$

147 where  $m$  is the summation index, and  $\Delta l$  is the path length per increment (here 7.56 km for 1s).  
148 For deriving the along-track magnetic field component,  $B_{AT}$ , we have subtracted from the  
149 CHAMP data the main field, crustal field and large-scale magnetospheric field, as represented  
150 by the high-resolution model POMME-6 (Maus et al., 2010). From the set of magnetic  
151 residuals, the component aligned with the velocity vector is calculated.

152 Zhou and Lühr (2017) derived net currents from integration along full CHAMP orbits. In  
153 addition, they applied integration loops confined to one hemisphere and could study  
154 hemispheric differences. Here we go one step further by estimating net currents flowing through  
155 a loop from subauroral latitudes up to the geomagnetic pole. In this way we get current estimates  
156 for all local times and can compare intensities on the dawnside with those on the duskside and  
157 noon with midnight results. The penalty for the further detailing of the results is that we have  
158 to make certain assumptions on the magnetic fields along parts of the integration path where no  
159 direct observations are available. The considered integration paths for the two local time sectors  
160 along the orbit are sketched in Figure 1. CHAMP magnetic field readings are taken from 50°  
161 magnetic latitude (MLat) (point A) up to the highest MLat reached along the orbit (point B).  
162 From there the virtual return path goes vertically down to point C, follows the Earth's surface  
163 until point D and goes vertically up to the start point A. The second loop follows the same  
164 scheme, taking CHAMP readings along the track from E to F and closing the path along the  
165 virtual track (F-G-H-E).

166 Since there are no measurements along the return path, we have to make assumptions about the  
167 magnetic field along that track. Here we follow the same reasoning and approach as



168 successfully applied in the work of Zhou and Lühr (2017). Auroral net currents are connected  
169 to FACs on both ends. According to Fukushima's theorem (Fukushima, 1976) magnetic  
170 signatures from a pair of antiparallel FACs closed by ionospheric currents vanish at the Earth's  
171 surface. The current configuration in our case, however, differs somewhat from the ideal case  
172 presented by Fukushima (1976), therefore the theorem might not be fully applicable here.

173 For estimating the contributions from the unsampled parts the following assumptions are made:  
174 (1) The contribution from C→D is similar in shape to that from A→B. (2) The contribution  
175 from D→A are proportional to the vertical field component  $B_z$  at point A since the radial  
176 magnetic field varies only smoothly through the current sheet. An outcome of this exercise is  
177 that the integral over A→B has to be multiplied by 1.2 for including the contributions from  
178 path C→D and that the vertical magnetic field component,  $B_z$ , has to be multiplied by 11 times  
179 the orbital altitude and divided by the permeability of free space to represent the contributions  
180 from path D→A. For further justification of these corrections see Zhou and Lühr (2017),  
181 Section 4.2. The same approach described here is also applied to the contour E-F-G-H-E. The  
182 remaining paths in the integration loops are B-C and E-H. Here again, the observed  $B_z$   
183 component at the points B (E) have been taken as a measure for scaling the missing  
184 contribution. We have tested a series of different factors multiplied to the  $B_z$  values at the top-  
185 side corners. There is a way to validate the suitability of the applied factors. Each local time  
186 sector is sampled in two ways, on upleg and 130 days later on downleg passes. In these two  
187 groups the ring integral is calculated in opposite directions. Only in the case of a proper scaling  
188 of this vertical contribution, both results are identical. From this test we found that the best  
189 agreement is obtained when the contributions from the vertical path elements in the middle are  
190 neglected. Figure 2 shows the final comparison for both hemispheres and all local times. For  
191 the northern hemisphere (left frame) we obtain in this way an almost perfect match between  
192 upleg and downleg results. The agreement is not as good for the southern hemisphere, but any  
193 additional contribution from these vertical paths makes the agreement between the curves  
194 worse.

195

### 196 3. Statistical survey of net current distribution

197 For obtaining the average distribution of net currents at all local times we consider CHAMP  
198 magnetic field data from the 5 years, 2001-2005. Overall 24,440 orbits with clean data are  
199 available. From each orbit we obtain two net current results for both hemispheres. This results  
200 in a large number ( $\sim 10^5$ ) of samples for this study. Figure 3 shows the average local time



201 variations of net currents in the northern and southern hemispheres (upleg and downleg results  
202 are combined). Positive values represent eastward currents. On average we find somewhat  
203 larger values in the northern hemisphere than in the southern. This is consistent with the  
204 observations of Zhou and Lühr (2017). Positive (eastward) net currents prevail within the local  
205 time sector 07-19 MLT, representing a dawn to dusk flow. The opposite sign is found in the  
206 other 12-hour local time sector, reflecting also dominant dawn to dusk currents.

207 There is not only a local time variation of the net currents but also a dependence on season.  
208 Figure 4 shows the distribution of current strength in a magnetic local time (MLT) versus Month  
209 of Year frame. We clearly find strongest currents during local summer months in particular  
210 around noon at both hemispheres. This is primarily due, as explained by Zhou and Lühr (2017),  
211 to the enhanced ionospheric conductivity during that season.

212 Another quantity that is expected to influence the net current, is the orientation of the  
213 interplanetary magnetic field (IMF). Here we have checked the dependence on the IMF  $B_y$   
214 component. As can be deduced from Figure 5, there is some dependence on the sign of IMF  
215  $B_y$ . For positive  $B_y$  clearly stronger net currents are observed in the northern hemisphere around  
216 the noon sector during months around June solstice. Our explanation for the difference in  
217 eastward net current is the DPY effect (e.g. Wilhelm et al., 1978; Clauer et al., 1995). The  
218 direction of this daytime auroral current depends on the sign of IMF  $B_y$ . For negative  $B_y$  it  
219 flows in opposite direction to the dawn to dusk currents in the polar cap. The related effect is  
220 also expected in the southern hemisphere but for negative  $B_y$  around December solstice. Here  
221 it is not so obvious. It seems that the period with positive IMF  $B_y$  were more active and thus  
222 masked the IMF  $B_y$  effect in the southern hemisphere.

223 As outlined by Zhou and Lühr (2017), the large net currents derived from noon/midnight  
224 orbits can be related to the cross-polar cap Pedersen currents closing the excessive Region 1  
225 (R1) FACs. The positive values around noon and the negative around midnight are both  
226 consistent with that notion. In this study we are more interested in the net currents on the  
227 dawn and dusk sides. Therefore, we consider the average values within the local time sectors  
228 03-09 MLT and 15-21 MLT as dawnside and duskside net currents, respectively. From Figure  
229 3 it is evident that a negative (westward) average current results from the 03-09 MLT sector  
230 and a positive (eastward) from the 15-21 MLT sector. This means, both sides contribute to an  
231 anti-sunward net current. The characteristics of these anti-sunward currents are of prime  
232 interest for this study.

233



#### 234 4. Dependence of net current on solar wind input and on season

235 Similar to Zhou and Lühr (2017) we also investigate the dependence of anti-sunward net  
236 currents on magnetic activity. Different from them we look at the fractions flowing on the  
237 dawn and dusk sides separately. As measure for the solar wind input, we use the coupling  
238 function as defined by Newell et al. (2007). By somewhat rescaling this function we obtain  
239 the so-called merging electric field,  $E_m$ , which represents approximately the solar wind  
240 electric field in units of mV/m

$$241 \quad E_m = \frac{1}{3000} V_{sw}^{\frac{4}{3}} (\sqrt{B_y^2 + B_z^2})^{\frac{2}{3}} \sin^{\frac{8}{3}}\left(\frac{\theta}{2}\right) \quad (3)$$

242 where  $V_{sw}$  is the solar wind velocity in km/s,  $B_y$  and  $B_z$  both in nT are the IMF components  
243 in GSM coordinates,  $\theta$  is the clock angle of the IMF.  $E_m$  values have been smoothed over 15  
244 min, and the propagation time from the bow shock to the ionosphere has been considered by a  
245 delay of 20 min (for more details see Zhou and Lühr, 2017).

246 Figure 6 shows the mean dependence of the eastward net currents on the dawn and dusk sides  
247 on the merging electric field,  $E_m$ , separately for the northern and southern hemispheres. The  
248 current values had been grouped into five activity classes ( $0 < E_m \leq 1$ ,  $1 < E_m \leq 2$ ,  $2 < E_m \leq 3.5$ ,  
249  $3.5 < E_m \leq 5$ ,  $5 < E_m \leq 7$  mV/m). Blue dots represent the mean values within these classes and the  
250 blue bars reflect the standard deviations. The mean values infer a good linear relationship  
251 between current intensity and merging electric field in all cases, as confirmed by the fitted red  
252 lines. On the dawnside westward currents get stronger with growing  $E_m$  and correspondingly  
253 eastward currents intensify on the duskside. This confirms in all four cases an increase of anti-  
254 sunward currents with growing activity. Slopes are somewhat steeper on the dawnside than on  
255 the duskside. Interestingly, the net currents on the dawnside show a small positive bias ( $\sim 52$   
256 kA) for vanishing solar wind input. We relate that to the effect of net anti-sunward plasma  
257 flows driven by intense day-to-night winds in the early morning sector (e.g. Lühr et al., 2007)  
258 during quiet periods.

259 As expected, the net currents on the flanks depend also on season. Figure 7 shows the annual  
260 variation of eastward net currents on the dawn and dusk sides separately for the two  
261 hemispheres. This analysis is based on data from more active periods with  $E_m > 3$  mV/m  
262 (approximately  $Kp > 4^+$ ) since anti-sunward net currents are phenomena increasing with  
263 magnetic activity. We find in both hemispheres weaker anti-sunward currents at local summer  
264 than at local winter. This holds for the dawn and dusk sides and is consistent with the results  
265 of Zhou and Lühr (2017). Compared to the mean values, the relative annual variations are not



266 too large (15% - 20%) and have comparable sizes in both hemispheres. In the northern  
267 hemisphere a semi-annual signature is quite prominent, commonly referred to as the Russel-  
268 McPherron effect (Russel and McPherron, 1973). It reflects the typical annual variation of  
269 magnetic activity with maxima at equinoxes and a minimum around June solstice. The semi-  
270 annual variation is not so obvious in the southern hemisphere, but the annual amplitude is  
271 larger.

272 For completeness we have also calculated the dependence of the dawn and dusk side net  
273 eastward currents on solar wind input separately for June and December solstice months and  
274 for the two hemispheres. Obtained results are listed in Table 1. The negative signs of the  
275 slopes on the dawnside and the positive on the duskside represent both increasing anti-  
276 sunward current intensity with enhanced solar wind input. When comparing the slopes of the  
277 dawn and dusk sides between the two solstices, one finds a smaller seasonal difference on the  
278 dawnside than on the duskside. Here the factor is partly reduced to less than a half during  
279 local summer with respect to local winter. Net currents in the dusk sector are obviously less  
280 dependent on solar wind input during times of a sunlit ionosphere. This is surprising since  
281 Guo et al. (2014) reports that the eastward auroral electrojet intensity shows a larger seasonal  
282 variation (stronger in local summer) than the westward jet. Obviously, the more pronounced  
283 conductivity gradients between the auroral region and the polar cap during dark seasons play  
284 a larger role for net currents. Finally, it is interesting to note that in Table 1 the intersects on  
285 the dawnside show systematically large sunward net currents (82 kA) in the summer  
286 hemispheres. This is consistent with the stronger day-to-night wind in the sunlit polar region  
287 (e.g. Lühr et al., 2007) which seem control the anti-sunward plasma flow over the dawnside  
288 polar cap during quiet times.

289

## 290 **5. Variation of net currents during a magnetic storm**

291 It is suggested since quite some time that the anti-sunward currents are connected via FACs to  
292 the ring current (e.g. Suzuki et al., 1985). In particular, it is believed that net currents feed the  
293 partial ring current on the duskside. Here we want to check, to which degree the CHAMP data  
294 support this inference. The partial ring current generally forms during the main phase of a  
295 magnetic storm.

296 For investigating these connections in more details, we have selected the geomagnetic storm  
297 on 17 August 2003. This event is well suited because CHAMP is crossing the auroral oval on  
298 orbits close to dawn/dusk. The storm is initiated by a sudden storm commencement (SSC) at



299 14:20 UT on 17 August. From the solar wind and interplanetary magnetic field (IMF)  
300 variations, shown in Figure 8 (bottom), we can deduce that a sudden increase of solar wind  
301 speed from about 420 km/s to more than 500 km/s is responsible for the SSC. About an hour  
302 later, when IMF  $B_z$  turns negative, the main phase of the storm starts and extends into the  
303 next day. On that day the storm time disturbance index reached a minimum of  $D_{ST} = -148$  nT  
304 (see Fig. 8, top frame). It follows a typical recovery phase lasting several days. During part of  
305 that time IMF  $B_z$  is still negative, but the solar wind speed has returned to pre-event levels.

306 For comparison we present in the top frame of Figure 8 the storm-time evolutions of the total  
307 anti-sunward net currents (blue curves) including contributions from both hemispheres  
308 together with the SYM-H index (red curves). The SYM-H values are averages over the 10-  
309 min intervals when CHAMP crossed the polar regions. Right after the southward turning of  
310 IMF  $B_z$  intense anti-sunward currents (negative values) commence. About 4 hours later  
311 currents recover to a moderate value, but intensify again early next morning. This intermittent  
312 occurrence of net current continues into the recovery phase of the storm but with decreasing  
313 amplitudes.

314 So far, we have seen the evolution of total net current intensity during the magnetic storm on  
315 17 August. More details can be derived from Figure 9, where the contributions from the two  
316 hemispheres are shown separately. The current signatures are quite different in the four  
317 sectors. Before the SSC net currents in all frames are close to zero. Particularly intense anti-  
318 sunward currents, up to 2 MA, appear in the southern hemisphere (SH) on the dawnside  
319 during the main phase. Some hours before this strong signal, less intense anti-sunward  
320 currents are observed on the dawnside in the northern hemisphere (NH) and the duskside SH.  
321 It is interesting to note that there is in general a synchronous variation of net currents in these  
322 two antipodal sectors with somewhat smaller amplitudes in the south. For example, the  
323 prominent negative peaks around 42h Event Time (ET) in both hemispheres, which occur at  
324 the start of the recovery phase. Even later in the recovery phase (~55h ET) a sizable anti-  
325 sunward current appears in the SH dawn sector. Different to the other sectors there is only  
326 little net current activity on the NH duskside. Quite common for all four sectors, there is  
327 hardly any net current activity during times of northward IMF.

328 For the interpretation of the observations we have to remind that the event takes place towards  
329 the end of northern summer. More intense anti-sunward currents are therefore expected in the  
330 SH. Also the quietness on the NH duskside is consistent with our previously shown statistical  
331 results for that season. The quasi-synchronous variation of net currents at NH dawn and SH



332 dusk could convincingly be explained with a control by IMF  $B_y$  on related FACs in the polar  
333 cap. Stronger anti-sunward currents are expected in the NH dawnside for negative IMF  $B_y$   
334 and in the SH dawnside for positive IMF  $B_y$ . A direct comparison with the IMF observations  
335 reveals a qualitative agreement. For example, the intense SH dawn current matches well the  
336 positive excursion of IMF  $B_y$  around 30h ET, but the details of phasing do not fit so well in  
337 other cases. At least for this event we can state that in both hemispheres more intense anti-  
338 sunward net currents are observed on the dawnside than on the duskside.

339 It would have been desirable to study more individual storms in this detail. But an event has  
340 to satisfy a number of conditions for providing instructive results on the temporal evolution of  
341 anti-sunward currents during a storm. The storm should occur close to one of the solstice  
342 seasons, and the local time of the CHAMP orbit has to be close to dawn/dusk. We have  
343 considered all storms during the CHAMP era (2000-2010) with  $D_{ST}$  exceeding -100 nT. Just  
344 the presented event satisfied all these requirements reasonably well.

345

## 346 **6. Ground-based signature related to anti-sunward net current**

347 The observed anti-sunward currents are connected on both ends to FACs. These field-aligned  
348 currents have to close somewhere in the magnetosphere. Depending on the route these  
349 currents take corresponding magnetic signatures are expected at Earth surface. Traditionally  
350 the  $D_{ST}$  index (or SYM-H, as shown in Figs. 8 and 9) is used for describing the evolution of a  
351 storm. But this index reflects only the azimuthally symmetrical part of the magnetospheric  
352 fields. Therefore, it is not well suited to reflect the asymmetric effects possibly caused by the  
353 auroral net currents. More appropriate for this purpose seems to be the SuperMAG ring  
354 current index, SMR. It is a quantity comparable to  $D_{ST}$  or SYM-H but provides local time  
355 resolution from four sectors (SMR-00, SMR-06, SMR-12, SMR-18). More details about the  
356 SMR index can be found in Newell and Gjerloev (2012). By comparing the evolution of  
357 magnetic signatures on the evening and morning sides (SMR-18 and SMR-06) we may see  
358 the effect of a partial ring current. Figure 10 shows in the top frame the field deflections in  
359 these two time sectors during our storm. As expected, there are larger amplitudes observed on  
360 the evening side, in particular towards the end of the main phase. In the lower frame the  
361 differences between the two traces, SMR-18 minus SMR-06, are plotted. In this way we try to  
362 eliminate the contribution of the symmetrical ring current. Before and after the active phase of  
363 the storm the difference stays close to zero. Shortly after the SSC we find first positive  
364 deflections, i.e. a dominance of the dawn sector, and at the end of the prominent minimum,



365 i.e. larger effects on the duskside. Thereafter the difference signal is more variable. A closer  
366 comparison between SMR difference signal and the net currents in Figure 9 reveals that the  
367 best (but not perfect) match is found with the SH dawnside currents. However, these would,  
368 according to the traditional picture weaken the ring current on the morning sector. At least for  
369 this storm the asymmetric  $D_{ST}$  effect cannot be explained by an intensification of the duskside  
370 ring currents. We will revisit this issue in the discussion, Section 7.

371 From our study of the anti-sunward net currents we know that the effects are significantly  
372 different in the two hemispheres mainly depending on the season. Although SMR provides  
373 information on local time differences, it does not distinguish between hemispheric sources.

374 In order to obtain more information on the net current seasonal effects in ground observations  
375 we analysed magnetic field data from a meridional chain of observatories. Stations involved  
376 are Wingst (WNG, 54.15° DLat), L'Aquila (AQU, 42.45° DLat), Tamanrasset (TAM, 24.80°  
377 DLat), Bangui (BNG, 4.36° DLat), and Hermanus (HER, -33.86° DLat), where DLat is the  
378 latitude in dipole coordinates. Our study has shown that net currents are particularly strong  
379 during magnetic storms. We are therefore interested in magnetic field deflections at the  
380 observatories during disturbed times. The disturbance signal is determined from times with a  
381 magnetic activity index  $K_p \geq 6$ . Here the values around 06 and 18 MLT are considered since  
382 they are expected to show the largest difference. For obtaining them we took the hourly  
383 averages of the horizontal component,  $H$ , from 04+05 UT and 16+17 UT, respectively. A  
384 quiet-time background field is subtracted, determined from hourly averages of the same UT  
385 times as above but only data within the  $K_p = 0-1$  range are selected. In order to make the  
386 result well comparable with our net currents we considered the same 5 years (2001-2005) as  
387 for CHAMP.

388 The obtained mean horizontal disturbance fields are listed in Table 2 separately for the three  
389 Lloyd seasons: June solstice (May-Aug), December solstice (Nov-Feb) and combined  
390 equinoxes (Mar+Apr, Sep+Oct). As expected, we get negative mean values (southward fields)  
391 in all the cases. The values in the evening sector are more negative than those from the  
392 morning sector. An exception makes the station WNG. Here all the dusk fields, opposed to  
393 the other observatories, are more positive than those from dawn. This observatory is located  
394 obviously too far north. Therefore, its readings are affected also by the auroral electrojet  
395 during severe storms, not only by the ring current. For that reason, we have not considered it  
396 any further in the analysis. The larger amplitudes at dusk than on the dawn side are  
397 traditionally attributed to the effect of the partial ring current. Overall means of  $H_{dawn} - H_{dusk}$



398 are: BNG: 83 nT, TAM: 73 nT, HER: 57 nT, AQU: 47 nT. The differences decrease with the  
399 distance from the geomagnetic equator.

400 The storm-time disturbance fields at the observatories vary from season to season. Largest  
401 values are obtained for the months around December and smallest around June. This reflects  
402 the distribution of strong storms during the 5 years considered. In order to find the relative  
403 level of disturbance at a given observatory, values have to be compared within a season. For  
404 this purpose, we selected BNG as the reference station because it is located close to the  
405 geomagnetic equator. Table 3 lists the ratios of the various stations separately for the seasons  
406 and the dawn and dusk sides. In principle, the expected trend emerges, observatories at higher  
407 latitudes record smaller disturbances. We have to note, however, that the data from BNG are  
408 partly quite disturbed. It seems, some instrumental problems have existed during those years,  
409 due to political unrest. This is in particular true for the dawn values. We tried to eliminate bad  
410 values from the sample. But still, the dawn references seem to be either a little low (equinox)  
411 or too high (June). Of interest is the relative decrease of the values with increasing latitude.  
412 When starting with the equinox seasons in Table 3 we find the expected order. This is not true  
413 for December solstice months. Here the highest latitude station AQU exhibits a larger ratio  
414 than HER. Conversely around June solstice, here the ratio at HER is much larger than at AQU  
415 and close to that at TAM.

416 For the interpretation of these ratio variations we like to recall the seasonal, hemispheric  
417 variations of the anti-sunward net currents, as shown in Figure 7. In both hemispheres the  
418 current strength peaks during local winter. This characteristic is also observed on ground;  
419 observatories in the winter hemisphere experience larger storm-time disturbance levels. The  
420 auroral field-aligned current systems feeding the anti-sunward net currents contribute also to  
421 mid-latitude magnetic signatures primarily in the same hemisphere.

422 The  $D_{ST}$  values are commonly interpreted as caused by a ring current in the equatorial plane.  
423 Therefore, a reduction of the deflection level with latitude is expected, proportional to  $\cos \beta$ ,  
424 where  $\beta$  is the magnetic dipole latitude. In Table 4 we compare the derived ratios of H  
425 deflections with the expected cosine values for our four stations. In this case the results are  
426 ordered by local summer and winter. The observed ratios in the winter hemisphere follow  
427 reasonably well the cosine law. Conversely, the summer results fall progressively short  
428 towards higher latitudes. Note, for June solstice, dawnside, we have deliberately used a 10%  
429 smaller reference than the BNG readings (see arguments above) to make the ratios of the



430 other three observatories more consistent. In the next section we will offer some suggestions  
431 for the reduced summer-time disturbance levels.

432 The ring current signal has also been measured by the *C/NOFS* satellite. On its low-latitude  
433 orbit (inclination:  $13^\circ$ ) it samples the H component deflections at all local times on every  
434 orbit. In that way, any azimuthal asymmetries of the signal can well be detected. In a  
435 dedicated study, Le et al. (2011) investigated the evolution of the ring current signals during  
436 several geomagnetic storms. They clearly could confirm the appearance of an asymmetry  
437 during the storm main phase. During the recovery phase the signal became symmetric again.  
438 In a later study Lühr et al. (2017) performed a statistical survey on the type of asymmetry. For  
439 different classes of magnetic activity, the mean difference between dawn and dusk deflections  
440 were determined and the local time where the maximum appeared. For high activity,  $Kp > 6$ ,  
441 they obtained a center displacement of 38 nT, half the difference between dawn and dusk  
442 signals. This can be compared with the difference of disturbance levels we derived here for  
443 periods of  $Kp > 6$  from the observatories. For BNG, closest to the equator, we got a mean  
444 value of 83 nT, which is slightly more than the corresponding result from *C/NOFS* (76 nT).  
445 The explanation for the difference between the two values could be the occurrence of larger  
446 storms during our analysis period (2001-2005) as compared to the years from 2009 through  
447 2013 considered for *C/NOFS* statistics. Interestingly, *C/NOFS* finds for all levels of activity  
448 largest ring current signals on average near 18 MLT. This suggests a large-scale 3D current  
449 system connected to the anti-sunward currents rather fixed in local time.

450

## 451 7. Discussion

452 In this study we investigated the statistical properties of anti-sunward net currents in the  
453 auroral regions and their relation to ground-based signatures at middle and low latitudes. The  
454 general properties of auroral net currents had been presented by Zhou and Lühr (2017). Here  
455 we go one step further by determining the anti-sunward currents flowing on the dawn and  
456 dusk sides separately. As expected, the current intensity is directly proportional to the solar  
457 wind coupling function,  $E_m$ . When looking at annual averages the resulting net currents are  
458 about the same for enhanced activity (e.g.  $E_m > 3$  mV/m) in the dawn and dusk sectors and in  
459 both hemispheres (see Fig. 7). However, obvious differences appear when taking the local  
460 seasons into account. From Table 1 we can deduce that the slopes of the current intensity  
461 curves with respect to  $E_m$  are similar on the dawn sides for local summer and local winter.  
462 Conversely on the duskside, the obtained  $E_m$  dependences are clearly steeper for winter than



463 for summer conditions. This is valid for both hemispheres. We interpret it as an indication  
464 that the conductivity gradient on the duskside between the auroral region and the polar cap is  
465 much steeper in the winter hemisphere than in the sunlit summer. Different from that  
466 dawnside conductivity gradients seem to be less season dependent.

467 When evaluating the average hemispheric net current characteristics from Table 1 we obtain  
468 for  $E_m = 6$  mV/m ( $Kp \approx 6^+$ ) intensities of about 640 kA and 810 kA in each hemisphere for  
469 summer and winter conditions, respectively. It has been reported earlier (e.g. Guo et al., 2014)  
470 that the intensity of the eastward electrojet on the duskside is depending more directly on the  
471 sun-induced conductivity. But we find, the stronger summer-time eastward electrojet  
472 obviously contributes less to the anti-sunward net currents. The closure of the electrojet  
473 currents across the polar cap seems to be quite efficient during the sunlit season.

474 A detail, interesting to note, is that for vanishing solar wind input,  $E_m = 0$ , i.e. due northward  
475 IMF, we obtain, in particular on the dawnside during summer season, sunward net currents of  
476 about 80 kA in both hemispheres. Reason for that is probably the day-to-night wind over the  
477 polar cap that is driving net currents in opposite direction. More dedicated studies would be  
478 needed for elucidating the details of a high-latitude wind dynamo under such special  
479 conditions.

480

#### 481 7.1 Comparison with ground-based observations

482 We have shown that the magnetic field effects of anti-sunward currents are also observable on  
483 ground. Our statistical study of recordings along a European-African meridional chain  
484 revealed that the high-latitude seasonal differences are visible on ground. The asymmetry  
485 between dawn and dusk disturbance signals during magnetically active periods is larger in the  
486 winter hemisphere, and the seasonal effect becomes more prominent at stations on higher  
487 latitudes. This strongly suggests that the full 3D current circuit, connected to the anti-sunward  
488 currents in each hemisphere, is contributing mainly to the mid-latitude magnetic signal in the  
489 same hemisphere. This means, recordings in the summer hemisphere underestimate the  $D_{ST}$   
490 value. The over-proportional reduction of the mean  $D_{ST}$  index during months around June  
491 solstice, compared to other activity indices, e.g.  $Kp$ , has earlier been reported (e.g. Mursula  
492 and Karinen, 2005). In their Figure 1 they show that the average H component deflection value  
493 at the northern hemisphere index observatories reaches almost 0 nT at the beginning of July.  
494 While at Hermanus the zero level is attained around new year. In our view the  $D_{ST}$  minimum  
495 can be explained by the combined effect of the well-known annual July magnetic activity



496 minimum with the weaker disturbance signal in the summer hemisphere. Since three out of  
497 four  $D_{ST}$  observatories are located in the northern hemisphere, the excessive July minimum in  
498  $D_{ST}$  is expected as resulting of a hemispheric bias. Just for completeness we may note that  
499 Mursula and Karinen (2005) offered another explanation for the  $D_{ST}$  July minimum that we  
500 do not regard as so convincing.

501 Rather interesting features are revealed from the event study of the magnetic storm on 17  
502 August 2003. The evolution of sunward currents, as shown in Figure 9, is quite different on  
503 the dawn and dusk sides in the two hemispheres. Several of the statistical features presented  
504 in the previous sections can also be found in this event that occurred during northern summer  
505 conditions. Largest currents are detected in the southern, winter hemisphere on the dawnside  
506 during the storm main phase. In the northern summer hemisphere the duskside currents  
507 exhibit only small amplitudes. This is consistent with the mean seasonal dependences of this  
508 local time sector (see Table 1). Sizable net currents appear on the dawnside in the northern  
509 hemisphere at times when they are low in the southern hemisphere. This hemispheric  
510 alternation in current flow can be related to the varying direction of the IMF  $B_y$  component.

511 For checking the magnetic effects of the net currents on ground we had a look at the SMR  
512 index for this event (see Fig. 10). We expected a clear dominance of SMR-18 over SMR-06.  
513 But only a moderate negative difference appears towards the end of the main phase in the  
514 lower frame of that figure. Over large parts of the storm-time the signal is varying about the  
515 zero-line. For the interpretation of this result we have to note that most of the observatories  
516 contributing to the SMR index are located in the northern hemisphere. Because of the  
517 prevailing summer season, the ring current index is expected to be underestimated (see Table  
518 4). This can be regarded as a general problem. Also for the determination of the  $D_{ST}$  value,  
519 three observatories in the northern hemisphere are used and one in the southern. This leads to  
520 a systematic underestimation of the ring current index during the months around June solstice  
521 compared to those from December months.

522 There is a certain anti-phase variation of the SMR difference in Figure 10 with the sunward  
523 currents in Figure 9 on the NH dawnside and SH duskside. Prominent peaks appear around  
524 19h and 41h ET in both figures but with opposite sign. This indicates that at the listed peak  
525 times the negative deflections in the northern hemisphere are stronger on the dawnside than  
526 on the duskside. The largest negative peak in the SMR difference signal, around 30h ET, is  
527 well aligned with the strong anti-sunward current on the SH dawnside, but it is not as large as  
528 expected from the strong net current in the SH. This observation provides clear evidence that



529 the effect of auroral net currents can directly be recognised by mid-latitude observatories, but  
530 the two hemispheres should be interpreted separately. With the present distribution of  
531 stations, contributing to SMR, however, it is expected that the asymmetry of the ring current  
532 effect is underestimated during the season around June solstice, like the presented case, when  
533 stronger anti-sunward currents flow in the southern hemisphere.

534

### 535 7.2 Suggestion for a 3D current circuit

536 When comparing the CHAMP net currents at the four quadrants with the temporal evolution  
537 of the SYM-H or SMR indices we find strongest net currents in the dawn sector and  
538 particularly in the southern, winter hemisphere (see Fig. 9) during the storm main phase. The  
539 traditional suggestion was that the auroral net currents, in particular those from the evening  
540 sector, are connected to the ring current and intensify the part in the dusk sector (e.g. Suzuki  
541 et al. 1985). But just on the duskside we find only weak anti-sunward currents during our  
542 August 2003 storm. In previous works the term “partial ring current effect” is frequently used.  
543 This was mainly meant as an acronym for an azimuthally asymmetric disturbance signal  
544 during magnetic storms. The presented observations in this paper and previous publications  
545 considering *in situ* ring current density distributions (see Lühr et al., 2017 for a review)  
546 provide little evidence for a direct connection between auroral net currents and the ring  
547 current. Here we want to introduce our idea of the 3D current circuit connected with the anti-  
548 sunward currents.

549 From electrodynamic considerations it can be assumed that the FACs connected to the net  
550 currents appear at steep conductivity gradients. This locates them at fairly high latitudes near  
551 the border between auroral oval and polar cap. Field lines from this border do not connect to  
552 the ring current but reach out close to the magnetopause. During the storm main phase a lot of  
553 current flows along the electrojets from the day to the night side, which cannot be returned to  
554 the dayside across the poorly conducting polar cap (in particular in the dark hemisphere). The  
555 excessive current flows out along field lines to the magnetopause on the dawn and dusk side  
556 flanks. Here it is conducted back to the dayside. Figure 11 presents a schematic drawing of  
557 the envisaged 3D current circuit. Shown is a view onto the northern hemisphere. Equivalent  
558 current routes are assumed on the southern side. There is no connection to the ring current  
559 foreseen.

560 A current through our dawnside circuit will generate a northward magnetic field on ground,  
561 thus reducing the  $D_{ST}$  effect. Conversely, net currents through the dusk loop cause a



562 southward field enhancing the ring current effect. Regardless on which side the net currents  
563 close the same kind of asymmetry results. The near-Earth disturbance signals from these  
564 current circuits are dominated by the magnetic effects of the connecting FACs. For the  
565 resulting signals, it does not make a big difference whether the currents close through the ring  
566 current or further out in the magnetopause. Support for our current model comes from  
567 Haaland and Gjerløv (2013), who report, based on Cluster observations, enhanced sunward  
568 magnetopause currents on the dusk flank during the main phase of a storm. With the 3D  
569 current circuit suggested here, it makes no problem to understand, why enhanced disturbance  
570 levels always appear around 18 MLT (see Le et al., 2011) independent of the magnetic  
571 activity level. Already Love and Gannon (2009) had noticed that storm-time disturbances are  
572 commonly higher around the 18 MLT sector. They even suggested a linear relation between  
573 the asymmetry amplitude and the  $D_{ST}$  value. The asymmetry should amount on average to  
574 about 20% of the  $D_{ST}$  value. This claim was challenged by Siscoe et al. (2012). These authors  
575 tried to identify a magnetospheric process that could systematically enhance the ring current  
576 intensity in the dusk sector. In the end they were not able to offer a convincing explanation.

577 We claim that our 3D current circuit, driven by the high-latitude net currents, can better  
578 explain the observed features of the asymmetry signal. It seems to be quite stable in space.  
579 Therefore, the localisation to 18 MLT is achievable. We do not believe in a dependence of the  
580 asymmetry amplitude on the  $D_{ST}$  value. The anti-sunward currents are closely controlled by  
581 the solar wind input ( $E_m$  value). But in a statistical sense,  $E_m$  and  $D_{ST}$  are related, therefore the  
582 result of Love and Gannon (2009) can be understood. We claim, there is no direct connection  
583 between the ring current activity and the asymmetric storm-time signal. More studies of  
584 magnetic fields and currents in the outer magnetosphere are needed to confirm our 3D current  
585 configuration.

586

## 587 **8. Summary and Conclusions**

588 In this study we have investigated the auroral net currents flowing anti-sunward. For the first  
589 time, we present the partitioning of contributions from the dawn and dusk sides and from the  
590 two hemispheres to the total net current. These magnetic storm-time phenomena show  
591 significant dependences on solar wind input, season, and IMF  $B_y$  orientation. Of particular  
592 interest here is the complete current circuit including the field-aligned currents attached to the  
593 anti-sunward currents and the closure in the magnetosphere. Important results may be  
594 summarised as follows:



- 595 1. Anti-sunward currents grow on average proportionally with the solar wind input (merging  
596 electric field,  $E_m$ ). This is valid for the dawn and dusk sides and for all seasons.
- 597 2. More intense currents are observed in the winter than in the summer hemisphere. We  
598 relate that to the steeper conductivity gradients between auroral zone and polar cap during  
599 dark seasons. Then a larger part of the electrojet return current has to be by-passed  
600 through the magnetosphere via FACs.
- 601 3. On average, more anti-sunward current is flowing on the dawnside (10%-20%). The  
602 seasonal dependence of net currents is larger on the duskside. In the sunlit summer  
603 hemisphere the intensity in this sector is greatly reduced compared to the values for  
604 winter conditions.
- 605 4. Event studies of magnetic storms confirm the connection between anti-sunward auroral  
606 currents and the asymmetric storm-time disturbance signal. From the event studied we see  
607 that this claim holds for the total net current. But the actual current track can change  
608 during a storm several times between dawn and dusk sides in the two hemispheres. Most  
609 responsible for the preferred path is the prevailing season but also the IMF  $B_y$  orientation.
- 610 5. Ground-based observations of the asymmetric disturbance signals confirm the seasonal  
611 dependence of larger values in the winter hemisphere. The horizontal disturbance  
612 component at the stations follows reasonably well the expected cosine-dependence with  
613 dipole latitude in the winter hemisphere. While for summer conditions a much faster  
614 reduction with latitude is observed. This hemispheric dependence implies a dominant role  
615 of the FAC magnetic fields for the asymmetric disturbance signals on ground.
- 616 6. We propose a 3D current system that connects during storm-times field-aligned currents  
617 with the anti-sunward high-latitude currents around noon and midnight and closes the  
618 loops through the magnetopause on the dawn and dusk flanks. We do not find evidence  
619 for a connection of this circuit with the ring current.

620 For confirming our claims about the large-scale current system causing the asymmetric storm-  
621 time magnetic disturbances more observations in the outer magnetosphere should be studied.

622

623 **Acknowledgements** The authors thank Ingo Michaelis for his great effort in improving the  
624 CHAMP Level 3 magnetic field data. The CHAMP mission was sponsored by the Space  
625 Agency of the German Aerospace Center (DLR) through funds of the Federal Ministry of  
626 Economics and Technology. The CHAMP magnetic field data (product identifier: CH-ME-3-  
627 MAG) are available at [ftp://magftp.gfz-potsdam.de/CHAMP/L3\\_DATA](ftp://magftp.gfz-potsdam.de/CHAMP/L3_DATA). The OMNI data is  
628 available at [ftp://spdf.gsfc.nasa.gov/pub/data/omni/high\\_res\\_omni/](ftp://spdf.gsfc.nasa.gov/pub/data/omni/high_res_omni/). The SMR data are  
629 downloaded from <http://supermag.jhuapl.edu/indices/>. The ground observations of magnetic



630 field are available at [www.intermagnet.org](http://www.intermagnet.org). The work of Yun-Liang Zhou is supported by the  
631 National Key R&D Program of China (No. 2018YFC1407303).

632

633

634

635

### References

- 636 Clauer, C. R., P. Stauning, T. J. Rosenberg, E. Friis-Christensen, P. M. Miller, R. J. Sitar  
637 (1995), Observations of a solar-wind-driven modulation of the dayside ionospheric  
638 *DPY* current system, *J. Geophys. Res.*, 100, 7697–7713.
- 639 Crooker, N. U. and G. L. Siscoe (1981), Birkeland Currents as the Cause of the Low-Latitude  
640 Asymmetric Disturbance Field, *J. Geophys. Res.*, 86, A13, 11,201–11,210.
- 641 Fukushima, N. (1976), Generalized theorem for no ground magnetic effect of vertical currents  
642 connected with Pedersen currents in the uniform-conductivity ionosphere, *Rept. Ionos.*  
643 *Space Res. Japan*, 30, 35–40.
- 644 Guo, J., Liu, H., Feng, X., Pulkkinen, T. I., Tanskanen, E. I., Liu, C., Zhong, D., and Wang,  
645 Y.: ML and seasonal dependence of auroral electrojets: IMAGE magnetometer  
646 network observations, *J. Geophys. Res.-Space*, 119, 3179–3188,  
647 <https://doi.org/10.1002/2014JA019843>, 2014.
- 648 Haaland, S. and J. Gjerløv (2013), On the relation between asymmetries in the ring current and  
649 magnetopause current. *J. Geophys. Res. Space Phys.* 118, 7593–7604  
650 [doi:10.1002/2013JA019345](https://doi.org/10.1002/2013JA019345)
- 651 Le, G., W. J. Burke, R. F. Pfaff, H. Freudenreich, S. Maus, and H. Lühr (2011), C/NOFS  
652 measurements of magnetic perturbations in the low-latitude ionosphere during  
653 magnetic storms, *J. Geophys. Res.*, 116, A12230, [doi:10.1029/2011JA017026](https://doi.org/10.1029/2011JA017026).
- 654 Love, J. J., and J. L. Gannon (2009), Revised Dst and the epicycles of magnetic disturbance:  
655 1958–2007, *Ann. Geophys.*, 27, 3101–3131.
- 656 Lühr, H., S. Rentz, P. Ritter, H. Liu and K. Häusler (2007), Average thermospheric wind  
657 patterns over the polar regions, as observed by CHAMP, *Ann. Geophys.*, 25, 1093–  
658 1101,  
659 [www.ann-geophys.net/25/1093/2007/](http://www.ann-geophys.net/25/1093/2007/).
- 660 Lühr, H., C. Xiong, N. Olsen, and G. Le (2017), Near-Earth magnetic field effects of large-  
661 scale magnetospheric currents, *Space Sci. Rev.* 206:521–545  
662 [doi:10.1007/s11214-016-0267-y](https://doi.org/10.1007/s11214-016-0267-y).
- 663 Maus, S., C. Manoj, J. Rauberg, I. Michaelis, and H. Lühr (2010), NOAA/NGDC candidate  
664 models for the 11th generation International Geomagnetic Reference Field and the  
665 concurrent release of the 6th generation POMME magnetic model, *Earth Planets*  
666 *Space*, 62, 729–735.
- 667 Mursula, K., and A. Karinen (2005), Explaining and correcting the excessive semiannual  
668 variation in the Dst index, *Geophys. Res. Lett.*, 32, L14107,  
669 [doi:10.1029/2005GL023132](https://doi.org/10.1029/2005GL023132).
- 670 Newell, P. T., T. Sotirelis, K. Liou, C.-I. Meng, and F. J. Rich (2007), A nearly universal  
671 solar wind-magnetosphere coupling function inferred from 10 magnetospheric state  
672 variables, *J. Geophys. Res.*, 112, A01206, [doi: 10.1029/2006JA012015](https://doi.org/10.1029/2006JA012015).

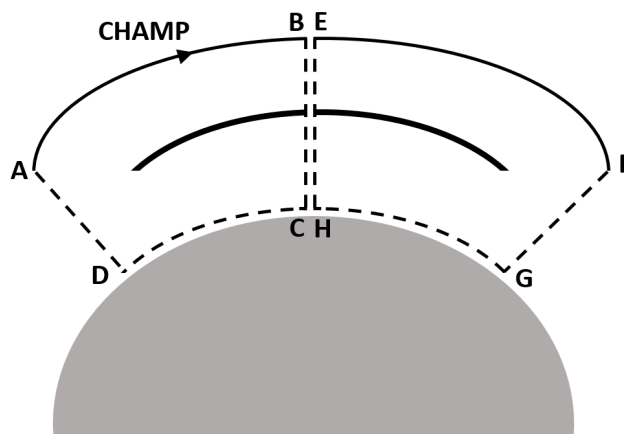


- 673 Newell, P. T., and J. W. Gjerloev (2012), SuperMAG-based partial ring current indices, *J.*  
674 *Geophys. Res.*, 117, A05215, doi:10.1029/2012JA017586.
- 675 Reigber, C., H. Lühr, and P. Schwintzer (2002), CHAMP mission status, *Adv. Space Res.*, 30,  
676 129–134, doi:10.1016/S0273-1177(02)00276-4.
- 677 [Rother, M.](#) and [Michaelis, I.](#) (2019): CH-ME-3-MAG - CHAMP 1 Hz combined magnetic  
678 field time series (Level 3). <https://doi.org/10.5880/GFZ.2.3.2019.004>
- 679 Russell, C. T., and R. L. McPherron (1973), Semiannual variation of geomagnetic activity, *J.*  
680 *Geophys. Res.*, 78, 92–108, doi:10.1029/JA078i001p00092
- 681 Siscoe, G. L., J. J. Love, and J. L. Gannon (2012), Problem of the Love-Gannon relation  
682 between the asymmetric disturbance field and Dst, *J. Geophys. Res.*, 117, A09216,  
683 doi:10.1029/2012JA017879.
- 684 Wilhelm, J., E. Friis-Christensen, T.A. Potemra (1978), The relationship between ionospheric  
685 and field-aligned currents in the dayside cusp, *J. Geophys. Res.*, 83, 5586–5594.
- 686 Stauning, P., and F. Primdahl (2000), First detection of global dawn-dusk ionospheric current  
687 intensities using Ampère’s integral law on Ørsted orbits, *Geophys. Res. Lett.*, 27,  
688 3273–3276, doi:10.1029/2000GL011954.
- 689 Suzuki, A., and N. Fukushima (1982), Sunward or anti-sunward electric current in space  
690 below the MAGSAT level, *Geophys. Res. Lett.*, 9, 345–347,  
691 doi:10.1029/GL009i004p00345.
- 692 Suzuki, A., and N. Fukushima (1984), Anti-sunward current below the MAGSAT level  
693 during magnetic storms, *J. Geomagn. Geoelectr.*, 36, 493–506, doi:10.5636/jgg.36.493
- 694 Suzuki, A., M. Yanagisawa, and N. Fukushima (1985), Anti-sunward space currents below  
695 the MAGSAT level during magnetic storms and its possible connection with partial  
696 ring current in the magnetosphere, *J. Geophys. Res.*, 90, 2465.
- 697 Zhou, Y.-L., and H. Lühr (2017), Net ionospheric currents closing field-aligned currents in  
698 the auroral region: CHAMP results, *J. Geophys. Res. Space Physics*, 122, 4436–4449,  
699 doi:10.1002/2016JA023090
- 700



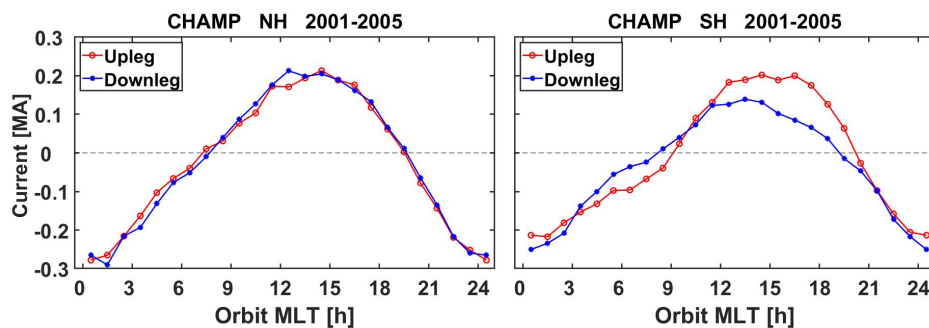
701  
702  
703

### Figures



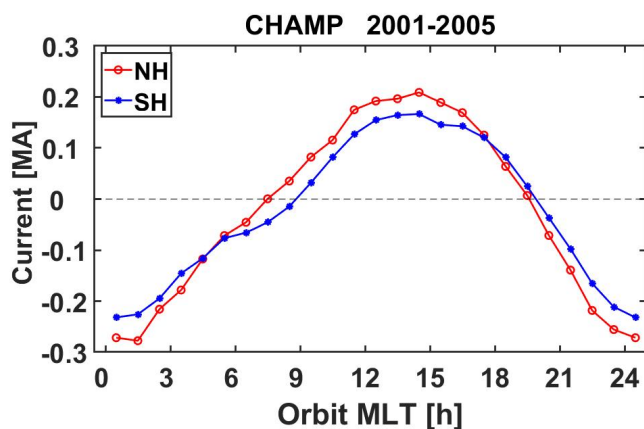
704  
705  
706  
707  
708  
709  
710  
711  
712  
713  
714  
715

**Figure 1.** Schematic drawing of the net current determination approach at auroral latitudes separately for dawn and dusk local time sectors. The unsampled virtual return paths are shown as dashed lines.



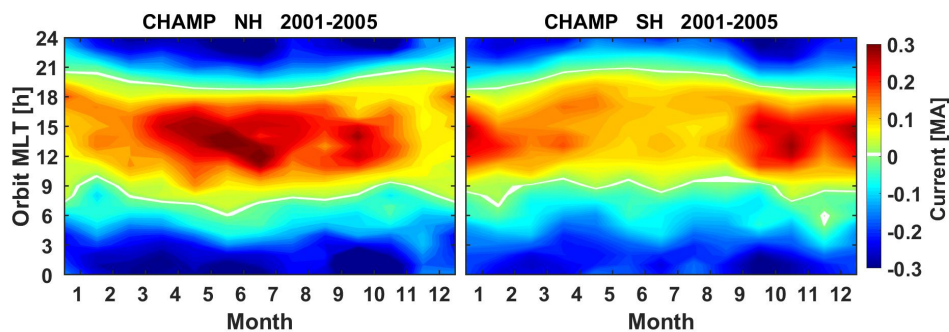
716  
717  
718  
719  
720  
721  
722  
723  
724  
725  
726

**Figure 2.** Local time dependence of auroral net currents separately for results from upleg and downleg passes. Best matches, shown here, are obtained when the contributions from the paths B-C and H-E are neglected.



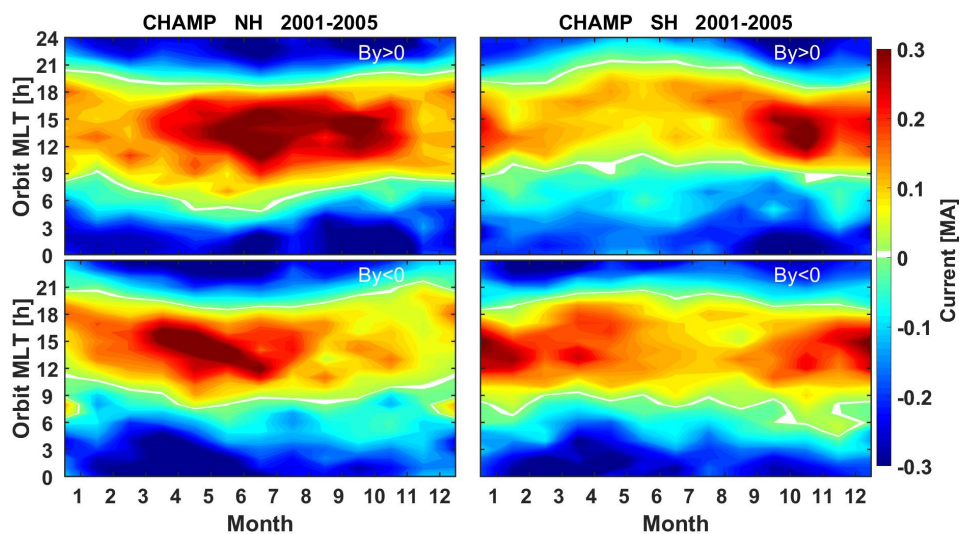
727  
728  
729  
730  
731  
732  
733  
734  
735  
736  
737

**Figure 3.** Local time dependence of mean auroral net currents; comparison between the two hemispheres.



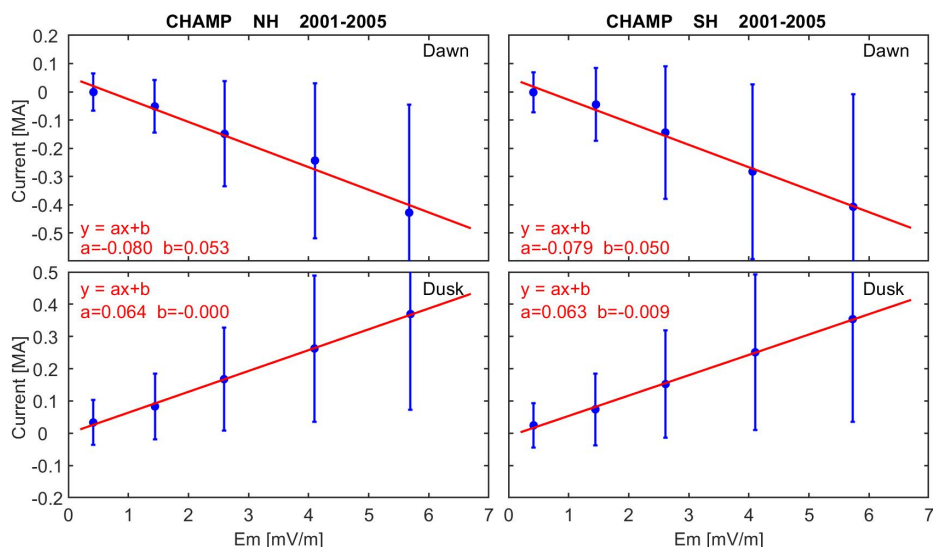
738  
739  
740  
741  
742  
743  
744  
745

**Figure 4.** Distribution of mean eastward net currents in local time versus Month of Year frames. Noon-time currents are strongest during local summer seasons.



746  
 747  
 748  
 749  
 750  
 751  
 752  
 753  
 754  
 755

**Figure 5.** Distribution of mean eastward net currents in local time versus Month of Year frames separately for positive and negative IMF  $B_y$  conditions. DBY currents have the same direction as the cross-polar cap currents for  $B_y > 0$  in the northern and  $B_y < 0$  in the southern hemisphere.

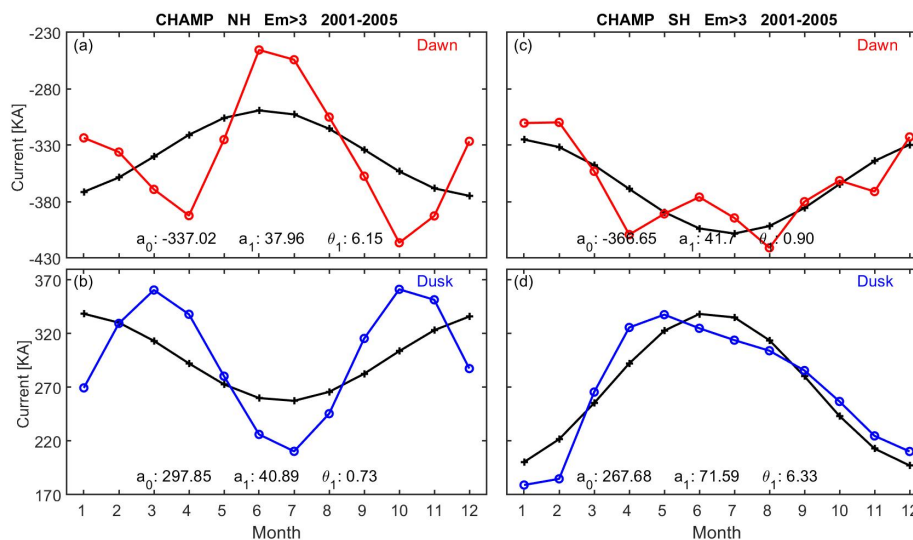


756  
 757  
 758  
 759  
 760  
 761  
 762

**Figure 6.** The  $E_m$  dependence of net currents on the dawn and dusk sides, separately for the Northern (left) and Southern (right) hemispheres. The solid dots with vertical bars indicate the mean values and standard deviation of the net eastward current for five levels of  $E_m$ . Parameters of the linear fits (red lines) are listed in the top left corner of each frame.



763



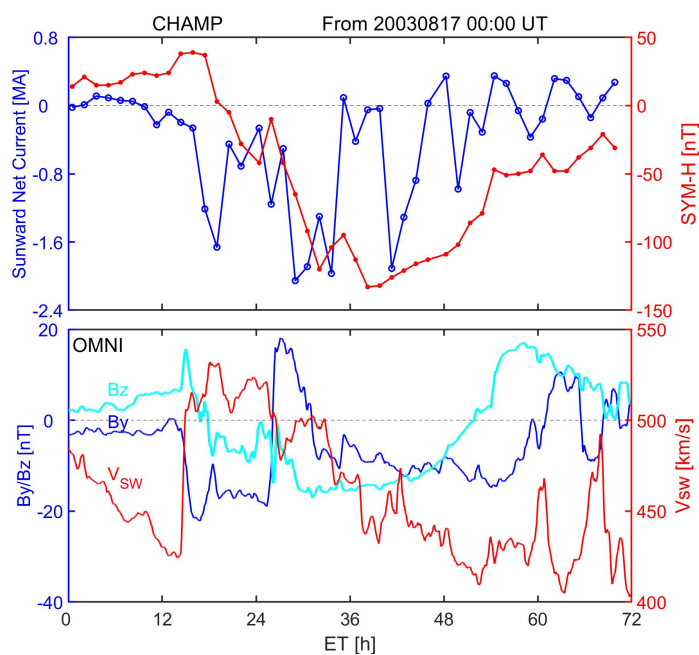
764  
765

**Figure 7.** The seasonal variation of eastward net currents. Presented are dawnside (top) and duskside (bottom) currents derived from high-latitude passes over the Northern (left) and Southern (right) Hemispheres. Black curves are sinusoidal fits to the observations. In each panel the constant term,  $a_0$ , annual amplitude,  $a_1$  (both in kA) and the phases the peaks,  $\theta_1$ , (in month) are listed.

771  
772  
773  
774



775

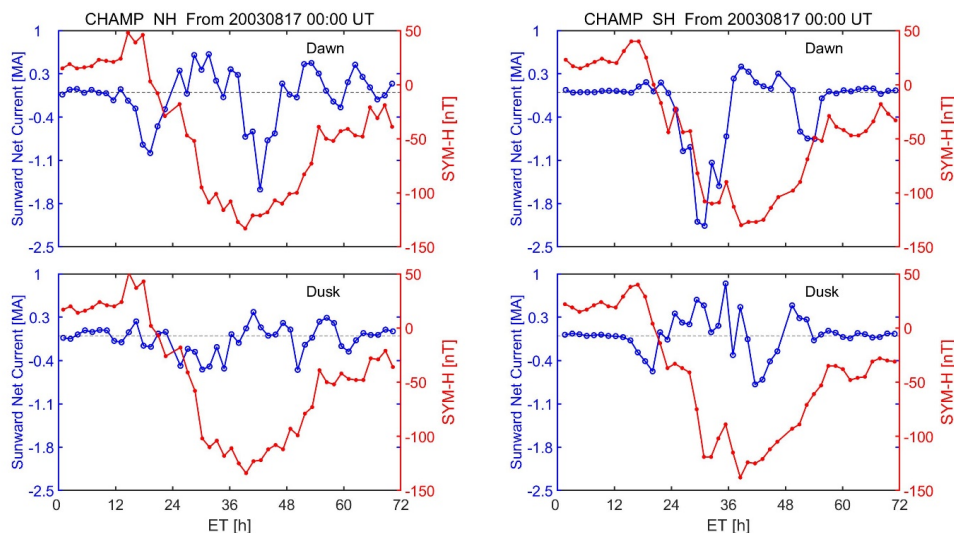


776  
777

778 **Figure 8.** (bottom) Solar wind velocity and interplanetary magnetic field components (GSM)  
779 variations for the storm starting on 17 August 2003. (top) The SYM-H index evolution during  
780 the storm and the total anti-sunward net current are shown for comparison.  
781

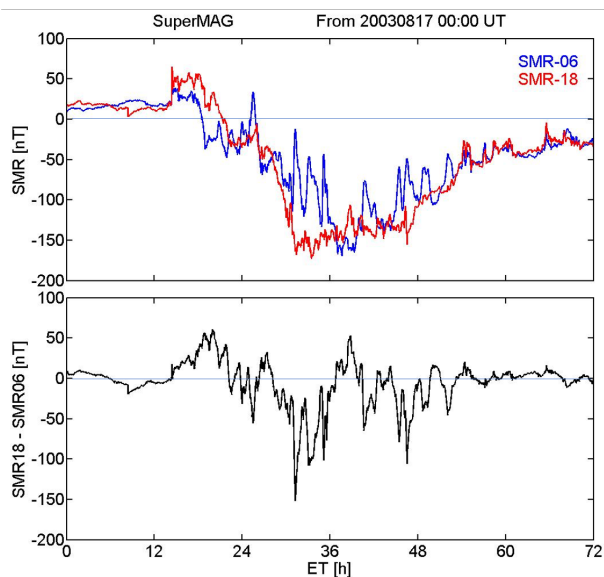


782



783  
784  
785  
786  
787  
788  
789  
790  
791  
792  
793

**Figure 9.** Temporal evolutions of the SYM-H index and the net currents separately for both hemispheres and for dawn and dusk sides during the storm 17-20 August 2003. Magnetic local time ranges are, NH dawn passes: 06-09 MLT, NH dusk passes: 17-21 MLT, SH dawn passes: 03-10 MLT, SH dusk passes: 17-23 MLT.

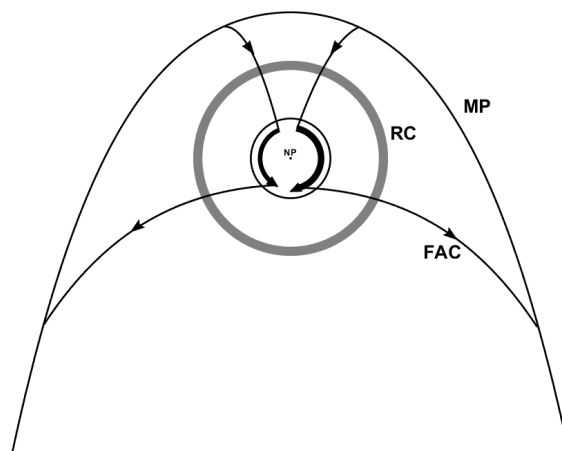


794  
795  
796  
797

**Figure 10.** (top) Temporal evolution of SMR storm-time index from the 06 and 18 local time sectors. (bottom) Differences between the two time sectors (SMR-06 – SMR-18).



798



799  
800

801 **Figure 11.** Schematic drawing of the suggested current circuits closing the high-latitude anti-  
802 sunward currents. Field-aligned currents rout the net from the polar cap boundary on the  
803 nightside to magnetopause on the dawn and dusk flanks. Here the currents flow sunward and  
804 return back from the dayside magnetopause to the cusp regions in both hemispheres.  
805



806  
 807  
 808  
 809  
 810  
 811  
 812  
 813  
 814  
 815  
 816  
 817  
 818  
 819  
 820  
 821  
 822  
 823  
 824  
 825  
 826  
 827  
 828  
 829  
 830  
 831  
 832

**Table 1.** The  $E_m$  dependence of the net eastward currents during June and December solstice months for both the dawn and dusk sides.

Season	Local time sector	Northern Hemis.		Southern Hemis.	
		Slope ( $10^6$ Am/V)	Inters. (kA)	Slope ( $10^6$ Am/V)	Inters. (kA)
Months: 05-08	Dawn	-78	83	-75	44
	Dusk	49	16	73	-18
Months: 11-02	Dawn	-69	26	-80	82
	Dusk	67	8	29	16

**Table 2.** The mean deflections of H component (in nT) at five observatories for different seasons during active times ( $K_p \geq 6$ )

Station	Local time	June	December	equinoxes
AQU	Dawn	-21.8	-97.5	-46.3
	Dusk	-71.3	-146.8	-88.3
HER	Dawn	-35.3	-77.2	-52.0
	Dusk	-104.8	-122.8	-106.0
BNG	Dawn	-50.6	-124.3	-59.4
	Dusk	-136.2	-205.9	-140.4
TAM	Dawn	-38.7	-109.7	-66.4
	Dusk	-112.2	-184.9	-127.0
WNG	Dawn	-43.9	-124.2	-46.3
	Dusk	6.5	-62.6	-21.5

833  
 834  
 835  
 836  
 837



838  
 839  
 840  
 841

**Table 3.** Ratio of mean disturbance deflection at a given observatory with respect to the value at the equator, separately for the three Lloyd seasons.

Station	DLat	Local time	June	December	Equinoxes
BNG	4.36°	Dawn	1	1	1
		Dusk	1	1	1
TAM	24.81°	Dawn	0.76	0.88	1.13
		Dusk	0.82	0.9	0.91
HER	-33.86°	Dawn	0.69	0.62	0.88
		Dusk	0.77	0.6	0.76
AQU	42.45°	Dawn	0.43	0.79	0.79
		Dusk	0.52	0.71	0.63

842  
 843  
 844  
 845  
 846  
 847  
 848  
 849  
 850  
 851  
 852

**Table 4.** Ratio of mean disturbance deflection at a given observatory with respect to the value at the equator, separately for the local seasonal conditions. Values can be compared with the latitude-dependent cosine law.

Station	DLat	Cosine law	Local summer		Local winter	
			Dusk	Dawn	Dusk	Dawn
BNG	4.36°	1	1	1.1	1	1
TAM	24.81°	0.91	0.82	0.84	0.9	0.88
HER	-33.86°	0.83	0.6	0.62	0.77	0.76
AQU	42.45°	0.75	0.52	0.47	0.71	0.79

853  
 854